

Thermal stability of multilayer graphene films synthesized by chemical vapor deposition and stained by metallic impurities

Yung Ho Kahng¹, Sangchul Lee², Woojin Park³, Gunho Jo⁴,
Minhyeok Choe³, Jong-Hoon Lee³, Hyunung Yu⁵, Takhee Lee⁴ and
Kwanghee Lee^{1,2,3}

¹ Research Institute for Solar and Sustainable Energies, Gwangju Institute of Science and Technology, Gwangju 500-712, Korea

² Department of Nanobio Materials and Electronics, Gwangju Institute of Science and Technology, Gwangju 500-712, Korea

³ School of Materials Science and Engineering, Gwangju Institute of Science and Technology, Gwangju 500-712, Korea

⁴ Department of Physics and Astronomy, Seoul National University, Seoul 151-747, Korea

⁵ Korea Research Institute of Standards and Science, Daejeon 305-340, Korea

E-mail: yhkahng@gist.ac.kr, tle@gist.ac.kr and klee@gist.ac.kr


Received 11 November 2011, in final form 2 January 2012

Published 20 January 2012

Online at stacks.iop.org/Nano/23/075702

Abstract

Thermal stability is an important property of graphene that requires thorough investigation. This study reports the thermal stability of graphene films synthesized by chemical vapor deposition (CVD) on catalytic nickel substrates in a reducing atmosphere. Electron microscopies, atomic force microscopy, and Raman spectroscopy, as well as electronic measurements, were used to determine that CVD-grown graphene films are stable up to 700 °C. At 800 °C, however, graphene films were etched by catalytic metal nanoparticles, and at 1000 °C many tortuous tubular structures were formed in the film and carbon nanotubes were formed at the film edges and at catalytic metal-contaminated sites. Furthermore, we applied our pristine and thermally treated graphene films as active channels in field-effect transistors and characterized their electrical properties. Our research shows that remnant catalytic metal impurities play a critical role in damaging graphene films at high temperatures in a reducing atmosphere: this damage should be considered in the quality control of large-area graphene films for high temperature applications.

 Online supplementary data available from stacks.iop.org/Nano/23/075702/mmedia

(Some figures may appear in colour only in the online journal)

1. Introduction

Graphene has attracted great interest because of its advantageous material properties, including high charge mobility, transparency, mechanical strength, and flexibility [1, 2]. Graphene has a theoretically achievable sheet resistance as low as 10–30 Ω/\square with mobilities as high as 200 000 $\text{cm}^2 \text{V}^{-1} \text{s}^{-1}$ [3, 4]. Accordingly, graphene is

expected to play a crucial role as a transparent and conductive electrode in electronic and optical devices [5], and studies have reported the application of graphene as electrodes in liquid crystal displays [6], organic memory devices [7, 8], organic field-effect transistors [9–11], light-emitting diodes [12–15], and organic solar cells [16–20].

To increase the applicability of graphene, a detailed understanding of its material properties is needed. In this

regard, researchers have investigated its specific mechanical properties and have found a trend toward higher strength in single-crystal graphene and lower strength in defective graphene [21–28]; similar trends have been observed for the corresponding electrical properties [22, 29–34]. The chemical properties of graphene have also been investigated in detail [35, 36]. In contrast, research on graphene's thermal stability is lacking. The high heat conductivity of graphene has been demonstrated by several researchers [37, 38], and its high thermal stability in vacuum or in an argon atmosphere has been reported [39, 40]. However, the thermal stability of large-area graphene synthesized by chemical vapor deposition (CVD) in a reducing atmosphere has not been investigated.

Thermal stability is an important property in graphene applications. For example, the use of graphene as a heat sink has been considered because of its high thermal conductivity [37, 38]. It has been shown that the process of thermal annealing is necessary to establish good electrical contact between graphene and metal electrodes in electronic devices [41, 42]. Thermal annealing of graphene is also used to remove the supporting polymer layer applied during the transfer of CVD-synthesized graphene [43, 44].

Recently, large-area graphene films with promising material properties have been synthesized by CVD on catalytic metal surfaces [45–62]. Ongoing research has revealed details regarding the role of source gases [54] and catalytic metal conditions [56, 57] in the quality of synthesized graphene films. In addition, the material properties of CVD-synthesized graphene have been investigated at the atomic level [55]. These detailed studies, combined with recent developments in roll-to-roll CVD synthesis [58] and low temperature CVD synthesis [59–62] for the mass production of graphene, show great potential for the future use of CVD-synthesized graphene in device applications.

This study reports the thermal stability of CVD-synthesized graphene films exposed to a reducing atmosphere. Catalytic nickel substrates were used for the synthesis. Using scanning electron microscopy (SEM), transmission electron microscopy (TEM), atomic force microscopy (AFM), and Raman spectroscopy, as well as electronic measurements, we show that CVD-grown graphene films are stable up to 700 °C in a reducing environment at atmospheric pressure. At 800 °C, the graphene films were damaged by etching induced by catalytic metal nanoparticles. At 1000 °C, the graphene films lost their flatness, and many tortuous tubes were formed, while carbon nanotubes (CNTs) were formed at the film edges and at catalytic metal-contaminated sites. In addition, the two-terminal resistance and the contact resistance between the graphene films and Ti/Au electrodes in graphene field-effect transistors were monitored using a pristine graphene and an 800 °C-annealed graphene film.

2. Experimental details

2.1. Graphene sample preparation

Graphene was synthesized on Si/SiO₂ (300 nm)/Ti (20 nm)/Ni (300 nm) substrates purchased from Jinsol, Inc. Graphene

films were synthesized on 1 × 1 cm² nickel substrates in a CVD chamber, with flows of 1.6 sccm methane, 208 sccm hydrogen, and 192 sccm argon for 5 m at 1000 °C and 760 Torr. Following synthesis, the graphene films were transferred from the nickel substrate by etching the nickel in an aqueous iron chloride (FeCl₃) solution (1 M) to Si/SiO₂ substrates for analysis and characterization. After the etching of the nickel catalyst, the graphene film was sequentially cleaned in DI water in three separate petri dishes. During transfer, a polymethyl-methacrylate (PMMA) coating was applied as a protective layer and was removed using acetone afterward. More details of the graphene sample preparation have been reported previously [9, 63].

Thermal treatment of the graphene samples was performed in a CVD chamber at 600–1000 °C for 5 m (unless stated otherwise) with flows of 6 sccm hydrogen and 144 sccm argon at 760 Torr.

2.2. Measurements

A Hitachi S-4700 field emission scanning electron microscope (FESEM) operating with an accelerating voltage of 10 kV was used to image the graphene samples. For the elemental analysis, we used a Horiba 7200-H energy dispersive x-ray spectroscope (EDX) on some graphene samples during the SEM imaging session. For the tilted SEM imaging, a Nova 200 dual-beam focused ion beam (FIB) apparatus from FEI Co. was used with a 5 kV accelerating voltage. This apparatus was also used for preparing samples for the cross sectional TEM images. For the TEM imaging, a Cs-corrected ARM 200F TEM from Jeol Co. was used with a 200 kV accelerating voltage. Raman spectroscopy measurements were performed using a DXR Raman Microscope system from Thermo Fisher Scientific Co. equipped with a diode laser source operating at 532 nm and 8 mW. The atomic force microscope used was an XE-100 system from Park Systems Inc. AFM scans were performed on a 20 × 20 μm² area at a typical scan rate of 0.5 Hz in noncontact mode. Hall measurements were performed using a Hall measurement system from Bio-Rad Inc. Measurements of the field-effect transistors with graphene stripes as active channels were performed using an Agilent Tech B1500A semiconductor device analyzer.

3. Results and discussion

Graphene films were thermally annealed at a high temperature (600–1000 °C) in a reducing atmosphere (flows of 6 sccm hydrogen and 144 sccm argon at 760 Torr), and the resulting structural changes were observed by SEM; the results are shown in figure 1. The images show that the graphene films change little up to 700 °C (denoted as 700-GR, figures 1(a) and (a1)). The 700-GR morphology was similar to that of the unheated graphene films (no-anneal-GR, image not shown). Our graphene films synthesized on Ni catalysts have thick multilayer domains (figures 1(a)–(c), dark areas) and thin areas with only a few layers (figures 1(a)–(c), lighter areas) [45–50]. When a graphene film was treated at 800 °C,

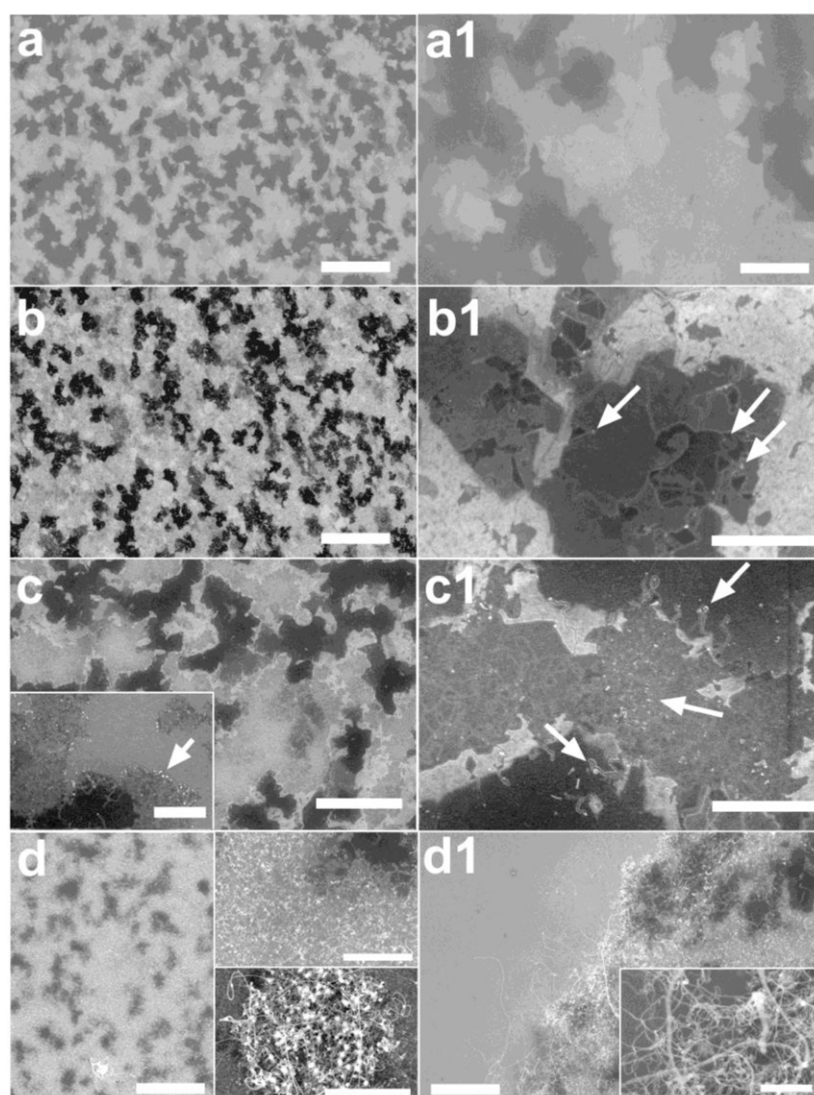


Figure 1. SEM images of graphene films annealed at various temperatures: (a) 700 °C, (b) 800 °C, (c) 900 °C, and (d) 1000 °C. Images indicated by a '1' are magnified more than the adjacent images on the left. Arrow marks are explained in the main text. Scale bar sizes: (a), (b), (d) 10 μm ; (c) 5 μm ; (c) inset, 1 μm ; (d) upper inset, 2 μm ; (d) lower inset, 5 μm ; (a1) 2 μm ; ((b1), (c1)) 1 μm ; (d1) 5 μm ; and (d1) inset, 0.5 μm .

however, it was damaged by the formation of narrow etched trenches all over the film (800-GR, figures 1(b) and (b1)). An increase in trench formation in conjunction with the rupture of some of the thin areas was observed in the 900 °C annealing treatment (900-GR, figures 1(c) and (c1)). At 1000 °C, the graphene began to deviate from flat; numerous tortuous tubes formed across the film, and carbon nanotubes (CNTs) formed at the edges on the perimeters of the films and at the catalytic metal-contaminated spots (1000-GR, figures 1(d) and (d1)). The morphological feature of 1000-GR is observed more clearly by tilted SEM and cross sectional TEM observations as the data show in figure 2.

AFM was also used to survey the morphological features of the graphene films, monitoring the development of surface roughness with increasing annealing temperature (see supplementary data, figures S1 and S2 available at stacks.iop.org/Nano/23/075702/mmedia). The morphological features

observed using AFM (figure S1 available at stacks.iop.org/Nano/23/075702/mmedia) were in agreement with the SEM observations shown in figures 1 and 2. The root-mean-square (RMS) roughness was nearly constant (~ 2.7 nm) up to an annealing temperature of 800 °C and increased significantly (4.7 ± 1.7 nm) at an annealing temperature of 900 °C (figure S2 available at stacks.iop.org/Nano/23/075702/mmedia). At 1000 °C, the graphene samples showed very rough surface features; some spots were as high as 1 μm due to the formation of tortuous tubes and CNTs on the film.

Our observation of graphene film damages at 800 °C differs from the results of previous studies [39, 40], which report that graphene films are stable up to 2300 °C in vacuum [40] and up to 2800 °C in an Ar atmosphere [39]. Damage to our CVD-synthesized graphene films began at much lower temperatures. We attribute this discrepancy to differences in the atmospheric conditions during thermal

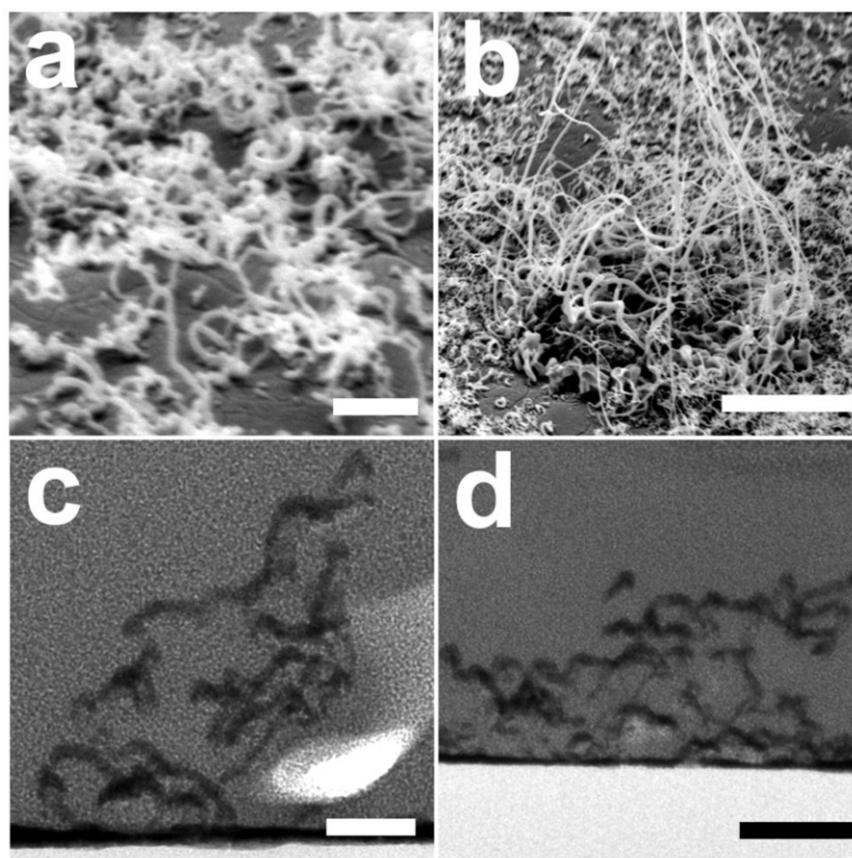


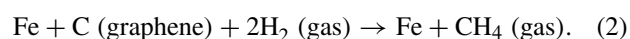
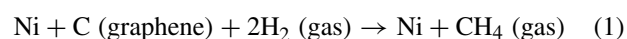
Figure 2. Tilted SEM (a), (b) and cross sectional TEM (c), (d) images of a graphene film annealed at 1000 °C. All the images were taken from one graphene sample. Before SEM imaging the sample was coated with a 16 nm thick Pt layer. For (a), (b) images, the samples stage was tilted by 56° from the e-beam direction. (a) The tortuous tubular structures observed on the film. (b) The long CNT-like structures observed on a metal-stained spot on the film. (c), (d) The cross sectional TEM images from an area similar to (a). In (c) and (d) the light-gray area at the bottom is the SiO₂ substrate layer, and the dark tortuous tubes coated by Pt particles could be observed in the gray background of a thick Pt layer deposited during the TEM sample preparation. Scale bar sizes: (a) 250 nm; (b) 2 μm; (c) 50 nm, and (d) 100 nm.

annealing. Our graphene films were heated in a flowing mixture of hydrogen (6 sccm) and argon (144 sccm) at 760 Torr.

Catalytic metal nanoparticles induced etching of our 800-GR films, which resulted in the formation of narrow trenches. Several pieces of experimental data support this conclusion: first, nanoparticles were observed at the terminal points of the trenches in the SEM images of 800-GR (figure 1(b1), indicated by arrows) and in the AFM images (figure S1(b1) available at stacks.iop.org/Nano/23/075702/mmedia, also marked by arrows); second, up to a few atom per cent of Fe and Ni were observed in some regions of our graphene films (1000-GR) via energy dispersive x-ray spectroscopy (EDX). Both metals were present because Ni is the substrate on which the graphene is grown and Fe is included in the etchant for the Ni. In addition, contaminated spots that contained a higher percentage of metal appeared sporadically in the graphene films (figure 1(d)). The existence of these metal elements in our graphene films indicates that the Ni etching and subsequent cleaning processes used during the transfer of graphene films to Si/SiO₂ surfaces are incomplete and do not fully eliminate metallic elements. For the nanoparticles to induce etching in the graphene film, they

need to contact the atmosphere. How such contacts are made is not understood clearly because both Fe and Ni contact the graphene film from underneath and the top surface is covered with PMMA during the transfer process. Maybe, defective holes in the graphene films and migration from the edges to the top surface of the graphene films during the PMMA removal process enabled the contact.

Graphene films etched by catalytic metal nanoparticles at high temperature have been previously reported by several groups [64–68]. Specifically, Ni nanoparticle-induced etching [64, 65] and Fe nanoparticle-induced etching [66, 67] in a reducing atmosphere and Ag nanoparticle-induced etching in air [68] have been reported. In these studies, metal-containing chemicals were applied to graphene samples at room temperature. Then, as the temperature increased, the chemicals decomposed to form metal nanoparticles on the graphene films. At high temperatures (650–1000 °C), these catalytic nanoparticles etched the graphene films by the chemical processes shown below [64, 67]:



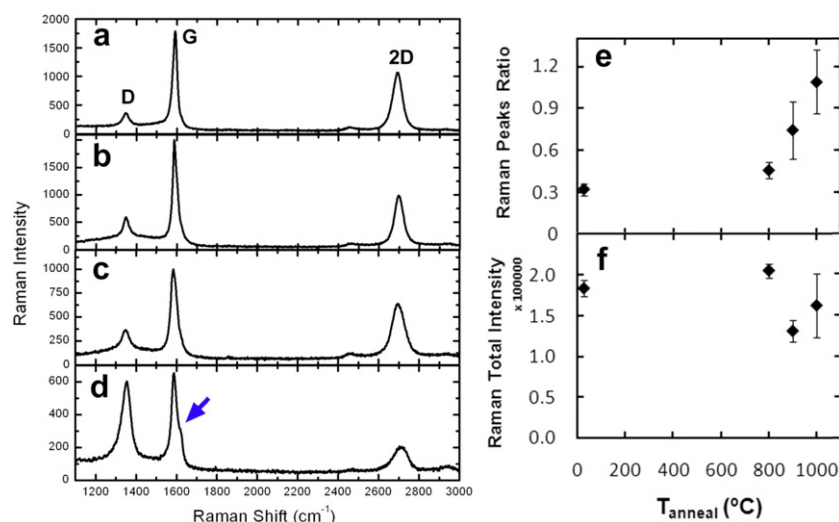


Figure 3. Raman spectra of graphene films annealed at various temperatures. Four to six spots were measured on each graphene film, and a representative spectrum is shown for the following annealing conditions: (a) no anneal, (b) 800 °C, (c) 900 °C, and (d) 1000 °C. (e) The D peak/G peak ratios and (f) the total intensities of the D, G, and 2D peaks.

Note that these processes are the reverse of the graphene synthesis processes.

Therefore, based on our observations and reference studies, we conclude that the key factors that contributed to the damage of the graphene films at 800 °C were the existence of remaining catalytic metal residues on the films and the exposure to an H₂ atmosphere. The combination of these two factors produced narrow-trench etching of the graphene films. Our results indicate that to increase the thermal stability of CVD-synthesized graphene films, either thorough cleaning of the graphene films to completely remove the metallic residue or avoidance of an H₂ atmosphere at high temperatures is required. These findings may be important for the potential application of graphene films as heat sinks [37, 38], for making good electrical contact between graphene and metal electrodes in electronic devices [41, 42] or for removing the supporting polymer layer used during the transfer of CVD-synthesized graphene by thermal annealing [43, 44].

When graphene films were annealed at 900 °C, more trenches were formed because of increased nanoparticle etching. Such increased etchings at higher temperature indicate that this process is thermally activated. Furthermore, ruptured areas appeared in some of the thinner areas containing only a few graphene layers (figures 1(c), (c1), and supplementary data, figures S1(c), (c1) available at stacks.iop.org/Nano/23/075702/mmedia). With a further increase of the annealing temperature to 1000 °C, the morphology of the graphene films was significantly altered; tortuous tubes formed across most of the film (figures 1(d) and (d) upper inset, and figure 2) and CNTs formed at the film edges (figure 1(d1)) and at sites of catalytic metal contamination (figures 1(d) and (d) lower inset, and figure 2(b)). The formation of CNTs at the metal-contaminated spots can be attributed to reactions induced by the catalytic metal particles. Formation of CNTs at the edges of the films also appears to be induced by the catalytic metal nanoparticles, because nanoparticle clustering at the edges was observed (figure 1(c)

inset, marked by an arrow). Such nanoparticle clustering at the edges may be induced by the stepped morphology which is more attractive for particle bindings and more difficult to clean than planar areas. CNT formation on graphene films induced by metal particles at high temperature was reported previously [64]. The mechanism for the formation of tortuous tubes in the film needs to be explained. It appears that if the amount of catalytic metal is not enough, carbon atoms in graphene cannot form the CNTs of familiar shape. We speculate that these tortuous tubes are formed by the rolling up of the edges of graphene nanoribbons. Such rolling up of graphene films during high temperature annealing has previously been observed [39] and theoretically explained [69]. Therefore, it is reasonable to propose that the tortuous tubes in the 1000-GR films were formed by the rolling up of the edges of many graphene nanoribbons that formed in the film by metallic nanoparticle etching, as observed in the 800-GR and the 900-GR films. Although the 1000-GR films had a different morphology compared with typical graphene films, they retained their graphitic properties within the film, according to our Raman measurement results (figure 3).

We monitored changes in the graphene films by thermal annealing using micro Raman spectroscopy, as shown in figure 3. For the Raman analysis, we monitored four–six spots on one sample from each thermal annealing treatment at varying annealing temperatures. Representative spectra are shown in figures 3(a)–(d). All of the measured graphene samples displayed D-band peaks near 1350 cm⁻¹, G-band peaks near 1580 cm⁻¹, and 2D-band peaks near 2700 cm⁻¹, which are well known to be indicative of graphene [70]. The higher G peak compared with the 2D peak in our Raman spectra reflects the multilayered nature of our graphene films. Additionally, the measured Raman spectra showed increasing D-band peak intensity with increasing annealing temperature, indicating that the defect density increased in the annealed films [70]. The observed increase in D-band intensity agrees

with our SEM and AFM observations reported above; i.e. more damage to the graphene films was observed at higher annealing temperatures. Statistical analysis of the D-band/G-band intensity ratio versus annealing temperature is shown in figure 3(e). Interestingly, the total Raman intensity (summation of D-, G-, and 2D-band intensities) was almost constant, despite the increase in annealing temperature (figure 3(f)), suggesting that the amount of graphitic material in the sample remained unchanged during annealing (approximately, the total intensity is proportional to the amount of graphitic material in the sample [70]). Therefore, even the 1000-GR films, which showed very different morphologies compared with the unheated graphene films, appeared to retain their graphitic properties. In some Raman spectra that were taken of areas in the 1000-GR film that included CNTs, a shoulder near 1620 cm^{-1} appeared on the G-band peak, as indicated by the arrow in figure 3(d). This shoulder formation can be explained either by the appearance of a D'-band peak, which is known to appear on damaged graphene films, or by G-band splitting, which is known to occur in metallic CNT samples [70].

Hall probe measurements [71] were also used to monitor changes in the electrical properties of the graphene samples following thermal annealing (figure 4). Similar to our previous results [63], the untreated graphene films showed a sheet resistance of $670 \pm 90\ \Omega/\square$ and a Hall mobility of $660 \pm 140\text{ cm}^2\text{ Vs}^{-1}$. These values did not deteriorate when the samples were annealed up to 700°C . In fact, the 700-GR film showed a slightly decreased sheet resistance of $470 \pm 110\ \Omega/\square$ and a slightly increased Hall mobility of $730 \pm 170\text{ cm}^2\text{ Vs}^{-1}$, probably because of the removal of some impurities remaining from the transfer process by thermal annealing [43]. The electrical property of the 800-GR films, however, deteriorated significantly because of the damage induced by nanoparticle etching, as discussed above. The 800-GR samples showed a sheet resistance of $2100 \pm 1400\ \Omega/\square$ and a Hall mobility of $178 \pm 98\text{ cm}^2\text{ V}^{-1}\text{ s}^{-1}$. These values did not change significantly in the samples that were annealed for longer periods (60 m) at the same temperature. The 900-GR samples deteriorated even more significantly, and only one out of three samples could be measured, giving values of $25\,800\ \Omega/\square$ and $9\text{ cm}^2\text{ V}^{-1}\text{ s}^{-1}$ for the sheet resistance and Hall mobility, respectively. None of the 1000-GR samples showed measurable electrical properties. Therefore, the Hall probe measurement results corroborate our SEM, AFM, and Raman observations.

To further investigate the effects of nanoparticle etching on the electrical properties of graphene films, we fabricated field-effect transistors (FETs) with patterned graphene stripes as active channels (figures 5(a)–(d)). The fabrication processes were similar to those reported previously involving a patterned Ni layer as a mask and graphene etching by O_2 -plasma treatment [9]. One no-anneal-GR sample and one 800-GR sample were used for the FET fabrication. A total of 15 FETs were fabricated per channel length, and four different channel lengths were employed: 50, 100, 150, and $200\ \mu\text{m}$, with a common width of $100\ \mu\text{m}$. Figures 5(e) and (f) show the typical transfer characteristics of $50\ \mu\text{m}$ -long

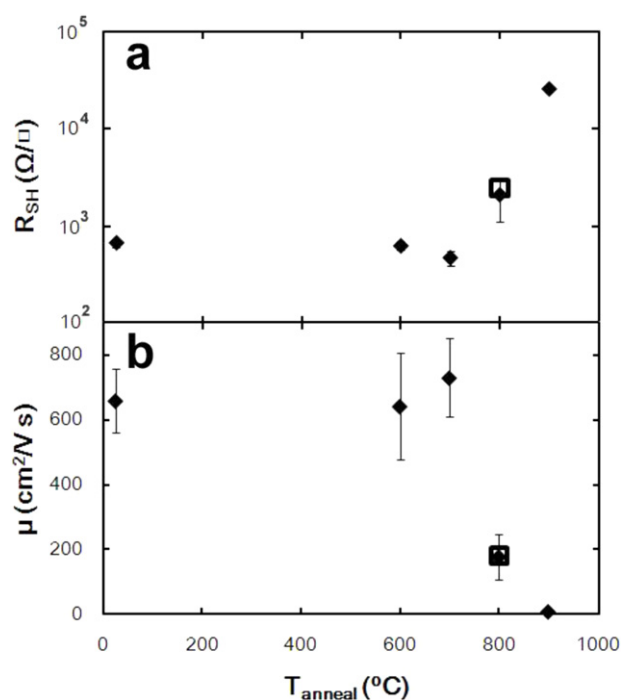


Figure 4. Electrical properties of the graphene films annealed at various temperatures: (a) sheet resistances and (b) Hall mobilities. The open square symbol represents a data point from a graphene sample annealed for 60 min, while filled diamonds represent the graphene samples annealed for 5 min.

FETs fabricated using the no-anneal-GR and the 800-GR film, respectively. FETs made with both graphene films showed weak p-type behavior, showing increasing resistance with increasing positive gate bias. This behavior was expected because our graphene films contained numerous multilayer domains distributed on a graphene background film that was a few layers thick and contained some defects [63]. It is known that the field effect of graphene is reduced as the number of layers increases [32] or the number of defect sites increases [30]. P-type behavior is induced by adsorption of impurities, such as water or oxygen [30, 72]. The increased resistance due to nanoparticle etching in the 800-GR was also observed in the FET devices. The FET made with 800-GR (figure 5(f)) showed a resistance four times higher than the FET fabricated with no-anneal-GR (figure 5(e)).

Further electrical characterization of the FET devices made with the two different graphene films (no-anneal-GR and 800-GR) was performed, and the results are shown in figure 6. The resistances of the FET devices with various channel lengths were obtained at different gate voltages, as shown in figures 6(a) and (c), and the transfer length method was used to obtain the contact resistance between the Ti/Au electrodes and no-anneal-GR (figure 6(b)) or 800-GR (figure 6(d)). The resistances of the FETs from the 800-GR film were 1.6–4 times higher than those of the FETs from the no-anneal-GR film. This significant increase agrees with our Hall measurement observations discussed above. However, the increase was not uniform. As observed in figure 6(c), the resistances with different channel lengths deviated from a linear trend. The resistances of the no-anneal-GR channel

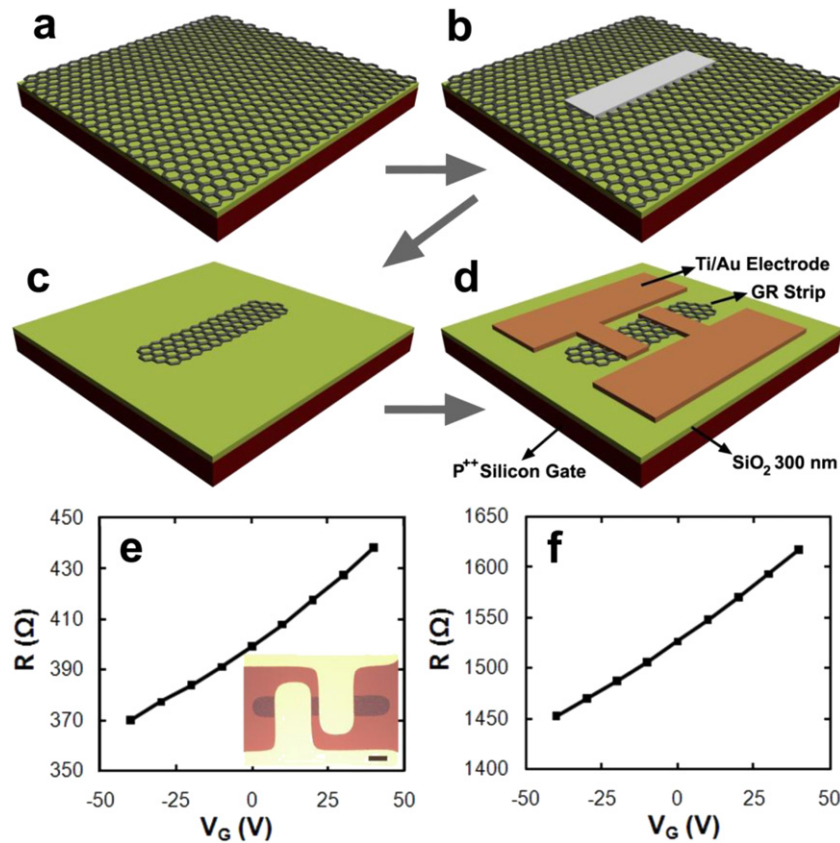


Figure 5. ((a)–(d)) The fabrication process for FETs with patterned graphene stripes as active channels: (a) graphene is transferred onto a Si/SiO₂ substrate, (b) a 50 nm thick Ni mask was deposited on the graphene by e-beam evaporation using a shadow mask, (c) a 100 μm-wide graphene stripe was patterned by O₂-plasma etching, followed by Ni removal in FeCl₃ solution and DI water washings, and (d) FETs were completed by the final deposition of Ti (20 nm)/Au (30 nm) electrodes. Resistance R versus gate voltage V_G plots taken on (e) a no-anneal-GR channel FET and (d) an 800-GR channel FET. The inset in (e) shows an optical microscope image of a 50 μm-long graphene channel FET. The scale bar is 100 μm.

FETs, however, were linearly aligned, as shown in figure 6(a). The scatter in the resistances of the 800-GR channel FETs is likely due to the nonuniform nanoparticle etching of the graphene film during thermal annealing. Our FET devices with four channel lengths were respectively distributed in four quadrants. Therefore, the FETs located in the quadrant where nanoparticle etching was more vigorous would have a larger resistance (e.g. 150 μm-long channel devices in figure 6(c)) compared with the FETs located in the quadrant with less nanoparticle etching (e.g. 100- and 200 μm-long channel FETs in figure 6(c)). The reason for such nonuniform etching is not clear, but may be due to the nonuniform distribution of remnant metallic impurities on the graphene films.

The average contact resistance of the no-anneal-GR channel FETs was $60 \pm 20 \Omega$ and varied little as the gate bias changed (figure 6(b)). This value yields a specific contact resistance of $2.4 \times 10^{-2} \Omega \text{ cm}^2$ (two $200 \times 100 \mu\text{m}^2$ contact areas in each FET), which is comparable to the previously reported values of 6×10^{-2} and $3 \times 10^{-4} \Omega \text{ cm}^2$ [41, 42]. In contrast, the contact resistances of the 800-GR channel FETs were approximately 1100 Ω (figure 6(d)), but this value is unreliable because the data points in the linear fit had errors as large as the measured values themselves (indicated by a double-sided arrow in figure 6(d)). Such large errors were

a result of the scattered resistance values from the 800-GR channel FETs.

4. Conclusions

In conclusion, graphene films synthesized by chemical vapor deposition on catalytic nickel substrates were found to be stable up to 700 °C in a reducing environment at atmospheric pressure. At higher temperatures, small amounts of catalytic metal impurities etched the graphene film, forming nanochannels at 800–900 °C. Tortuous tubular structures and carbon nanotubes were formed at 1000 °C. Correspondingly, the resistance and Hall mobility of the graphene deteriorated as the annealing temperature increased beyond 700 °C. The measurements of field-effect devices with channels made from an 800 °C-annealed graphene film showed increased resistances, as well as effects due to the nonuniform etching of the graphene film. These findings may have implications for the potential applications of graphene films as heat sinks, for making good electrical contact between graphene and metal electrodes, or for thermal removal of supporting polymer layers used during the transfer of graphene.

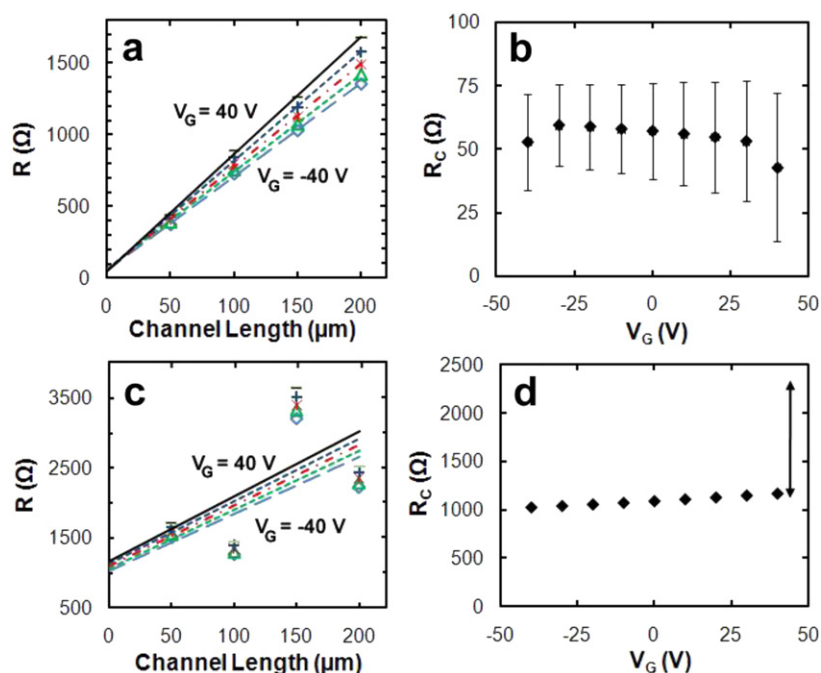


Figure 6. Measurement results for the FETs. The results are from the FETs made using (a), (b) no-anneal-GR film and (c), (d) 800-GR film. (a), (c) R versus channel length plots at various V_G values from -40 to 40 V at 20 V intervals. The contact resistance R_C values were obtained from the y-intercept of the linear fits to these plots. (b), (d) The R_C at various V_G values. Error bars are shown in (b). On (d), a double arrow indicates the size of the error bars.

Acknowledgments

This work was supported by the Core Technology Development Program for Next-Generation Solar Cells of the Research Institute for Solar and Sustainable Energies (RISE) at GIST and by a Korean National Core Research Center grant from the Korean Ministry of Education, Science, and Technology. We thank Mr Chang-Jun Lee in the Photonics Research Facility Center at GIST for help in operating the FESEM and EDX, and Mr Yun Chang Park and Ms Kyung Jin Park at the National Nanofab Center for help in operating the TEM and the FIB.

References

- [1] Geim A K 2009 *Science* **324** 1530–4
- [2] Geim A K and Novoselov K S 2007 *Nature Mater.* **6** 183–91
- [3] Chen J-H, Jang C, Xiao S, Ishigami M and Fuhrer M S 2008 *Nature Nanotechnol.* **3** 206–9
- [4] De S and Coleman J N 2010 *ACS Nano* **4** 2713–20
- [5] Wassei J K and Kaner R B 2010 *Mater. Today* **13** 52–9
- [6] Blake P et al 2008 *Nano Lett.* **8** 1704–8
- [7] Liu J, Yin Z, Cao X, Zhao F, Lin A, Xie L, Fan Q, Boey F, Zhang H and Huang W 2010 *ACS Nano* **4** 3987–92
- [8] Yu W J, Chae S H, Lee S Y, Duong D L and Lee Y H 2011 *Adv. Mater.* **23** 1889–93
- [9] Lee S, Jo G, Kang S-J, Wang G, Choe M, Park W, Kim D-Y, Kahng Y H and Lee T 2011 *Adv. Mater.* **23** 100–5
- [10] Shin W C, Seo S and Cho B J 2011 *Appl. Phys. Lett.* **98** 153505
- [11] Lee W H, Park J, Sim S H, Jo S B, Kim K S, Hong B H and Cho K 2011 *Adv. Mater.* **23** 1752–6
- [12] Wu J, Agrawal M, Becerril H A, Bao Z, Liu Z, Chen Y and Peumans P 2009 *ACS Nano* **4** 43–8
- [13] Sun T, Wang Z L, Shi Z J, Ran G Z, Xu W J, Wang Z Y, Li Y Z, Dai L and Qin G G 2010 *Appl. Phys. Lett.* **96** 133301
- [14] Lee J M, Jeong H Y, Choi K J and Park W I 2011 *Appl. Phys. Lett.* **99** 041115
- [15] Jo G et al 2010 *Nanotechnology* **21** 175201
- [16] Choe M et al 2010 *Org. Electron.* **11** 1864–9
- [17] Jo G et al 2010 *Appl. Phys. Lett.* **97** 213301
- [18] Park H, Rowehl J A, Kim K K, Bulovic V and Kong J 2010 *Nanotechnology* **21** 505204
- [19] Wang Y, Tong S W, Xu X F, Özyilmaz B and Loh K P 2011 *Adv. Mater.* **23** 1514–8
- [20] Lee Y-Y, Tu K-H, Yu C-C, Li S-S, Hwang J-Y, Lin C-C, Chen K-H, Chen L-C, Chen H-L and Chen C-W 2011 *ACS Nano* **5** 6564–70
- [21] Lee C, Wei X, Kysar J W and Hone J 2008 *Science* **321** 385–8
- [22] Gomez-Navarro C, Burghard M and Kern K 2008 *Nano Lett.* **8** 2045–9
- [23] Jiang J-W, Wang J-S and Li B 2009 *Phys. Rev. B* **80** 113405
- [24] Lee C, Wei X, Li Q, Carpick R, Kysar J W and Hone J 2009 *Phys. Status Solidi b* **246** 2562–7
- [25] Wong C-L, Annamalai M, Wang Z-Q and Palaniapan M 2010 *J. Micromech. Microeng.* **20** 115029
- [26] Neek-Amal M and Peeters F M 2010 *Phys. Rev. B* **81** 235421
- [27] Neek-Amal M and Peeters F M 2010 *Phys. Rev. B* **81** 235437
- [28] Ruiz-Vargas C S, Zhuang H L, Huang P Y, van der Zande A M, Garg S, McEuen P L, Muller D A, Hennig R G and Park J 2011 *Nano Lett.* **11** 2259–63
- [29] Du X, Skachko I, Barker A and Andrei E Y 2008 *Nature Nanotechnol.* **3** 491–5
- [30] Kim K, Park H J, Woo B-C, Kim K J, Kim G T and Yun W S 2008 *Nano Lett.* **8** 3092–6
- [31] Castro Neto A H, Guinea F, Peres N M R, Novoselov K S and Geim A K 2009 *Rev. Mod. Phys.* **81** 109–54
- [32] Craciun M F, Russo S, Yamamoto M, Oostinga J B, Morpurgo A F and Tarucha S 2009 *Nature Nanotechnol.* **4** 383–8

- [33] Peres N M R 2009 *J. Phys.: Condens. Matter* **21** 323201
- [34] Yazyev O V and Louie S G 2010 *Nature Mater.* **9** 806–9
- [35] Park S and Ruoff R S 2009 *Nature Nanotechnol.* **4** 217–24
- [36] Eda G and Chhowalla M 2010 *Adv. Mater.* **22** 2392–415
- [37] Seol J H *et al* 2010 *Science* **328** 213–6
- [38] Balandin A A 2011 *Nature Mater.* **10** 569–81
- [39] Campos-Delgado J *et al* 2009 *Chem. Phys. Lett.* **469** 177–82
- [40] Kim K, Regan W, Geng B, Aleman B, Kessler B M, Wang F, Crommie M F and Zettl A 2010 *Phys. Status Solidi RRL* **4** 302–4
- [41] Nagareddy V K, Nikitina I P, Gaskill D K, Tedesco J L, Myers-Ward R L, Eddy C R, Goss J P, Wright N G and Horsfall A B 2011 *Appl. Phys. Lett.* **99** 073506
- [42] Robinson J A, LaBella M, Zhu M, Hollander M, Kasarda R, Hughes Z, Trumbull K, Cavalero R and Snyder D 2011 *Appl. Phys. Lett.* **98** 053103
- [43] Cheng Z, Zhou Q, Wang C, Li Q, Wang C and Fang Y 2011 *Nano Lett.* **11** 767–71
- [44] Bhaviripudi S, Jia X, Dresselhaus M S and Kong J 2010 *Nano Lett.* **10** 4128–33
- [45] Reina A, Jia X, Ho J, Nezich D, Son H, Bulovic V, Dresselhaus M S and Kong J 2009 *Nano Lett.* **9** 30–5
- [46] Reina A, Thiele S, Jia X, Bhaviripudi S, Dresselhaus M S, Schaefer J A and Kong J 2009 *Nano Res.* **2** 509–16
- [47] Thiele S, Reina A, Healey P, Kedzierski J, Wyatt P, Hsu P-L, Keast C, Schaefer J and Kong J 2010 *Nanotechnology* **21** 015601
- [48] Chae S J *et al* 2009 *Adv. Mater.* **21** 2328–33
- [49] Kim K S, Zhao Y, Jang H, Lee S Y, Kim J M, Kim K S, Ahn J-H, Kim P, Choi J-Y and Hong B H 2009 *Nature* **457** 706–10
- [50] Lee Y, Bae S, Jang H, Jang S, Zhu S-E, Sim S H, Song Y I, Hong B H and Ahn J-H 2010 *Nano Lett.* **10** 490–3
- [51] Bae S *et al* 2010 *Nature Nanotechnol.* **5** 574–8
- [52] Li X *et al* 2009 *Science* **324** 1312–4
- [53] Levendorf M P, Ruiz-Vargas C S, Garg S and Park J 2009 *Nano Lett.* **9** 4479–83
- [54] Vlasiouk I, Regmi M, Fulvio P, Dai S, Datskos P, Eres G and Smirnov S 2011 *ACS Nano* **5** 6069–76
- [55] Yu Q *et al* 2011 *Nature Mater.* **10** 443–9
- [56] Yoshii S, Nozawa K, Toyoda K, Matsukawa N, Odagawa A and Tsujimura A 2011 *Nano Lett.* **11** 2628–33
- [57] Chen S, Cai W, Piner R D, Suk J W, Wu Y, Ren Y, Kang J and Ruoff R S 2011 *Nano Lett.* **11** 3519–25
- [58] Hesjedal T 2011 *Appl. Phys. Lett.* **98** 133106
- [59] Kim Y, Song W, Lee S Y, Jeon C, Jung W, Kim M and Park C-Y 2011 *Appl. Phys. Lett.* **98** 263106
- [60] Kim J, Ishihara M, Koga Y, Tsugawa K, Hasegawa M and Iijima S 2011 *Appl. Phys. Lett.* **98** 091502
- [61] Li Z, Wu P, Wang C, Fan X, Zhang W, Zhai X, Zeng C, Li Z, Yang J and Hou J 2011 *ACS Nano* **5** 3385–90
- [62] Jeon I, Yang H, Lee S-H, Heo J, Seo D H, Shin J, Chung U-I, Kim Z G, Chung H-J and Seo S 2011 *ACS Nano* **5** 1915–20
- [63] Kahng Y H, Lee S, Choe M, Jo G, Park W, Yoon J, Hong W-K, Cho C H, Lee B H and Lee T 2011 *Nanotechnology* **22** 045706
- [64] Campos L C, Manfrinato V R, Sanchez-Yamagishi J D, Kong J and Jarillo-Herrero P 2009 *Nano Lett.* **9** 2600–4
- [65] Ci L, Song L, Jariwala D, Elías A L, Gao W, Terrones M and Ajayan P M 2009 *Adv. Mater.* **21** 4487–91
- [66] Tsukamoto T and Ogino T 2011 *J. Phys. Chem. C* **115** 8580–5
- [67] Datta S S, Strachan D R, Khamis S M and Johnson A T C 2008 *Nano Lett.* **8** 1912–5
- [68] Severin N, Kirstein S, Sokolov I M and Rabe J P 2008 *Nano Lett.* **9** 457–61
- [69] Ivanovskaya V V, Zobelli A, Wagner P, Heggie M I, Briddon P R, Rayson M J and Ewels C P 2011 *Phys. Rev. Lett.* **107** 065502
- [70] Ferrari A C 2007 *Solid State Commun.* **143** 47–57
- [71] van der Pauw L J 1958 *Philips Res. Rep.* **13** 1–9
- [72] Schedin F, Geim A K, Morozov S V, Hill E W, Blake P, Katsnelson M I and Novoselov K S 2007 *Nature Mater.* **6** 652–5